



Cite this: *Nanoscale*, 2019, **11**, 1626

## Tailored Ag–Cu–Mg multielemental nanoparticles for wide-spectrum antibacterial coating†

Giulio Benetti,<sup>a,b</sup> Emanuele Cavaliere,<sup>a</sup> Rosaria Brescia,<sup>c</sup> Sebastian Salassi,<sup>d</sup> Riccardo Ferrando,<sup>d</sup> André Vantomme,<sup>e</sup> Lucia Pallecchi,<sup>f</sup> Simona Pollini,<sup>g</sup> Selene Boncompagni,<sup>f</sup> Beatrice Fortuni,<sup>h</sup> Margriet J. Van Bael,<sup>b</sup> Francesco Banfi<sup>i</sup> and Luca Gavioli<sup>i,\*a</sup>

Bactericidal nanoparticle coatings are very promising for hindering the indirect transmission of pathogens through cross-contaminated surfaces. The challenge, limiting their employment in nosocomial environments, is the ability of tailoring the coating's physicochemical properties, namely, composition, cytotoxicity, bactericidal spectrum, adhesion to the substrate, and consequent nanoparticles release into the environment. We have engineered a new family of nanoparticle-based bactericidal coatings comprising Ag, Cu, and Mg and synthesized by a green gas-phase technique. These coatings present wide-spectrum bactericidal activity on both Gram-positive and Gram-negative reference strains and tunable physicochemical properties of relevance in view of their "on-field" deployment. The link between material and functional properties is rationalized based on a multidisciplinary and multitechnique approach. Our results pave the way for engineering biofunctional, fully tunable nanoparticle coatings, exploiting an arbitrarily wide number of elements in a straightforward, eco-friendly, high-throughput, one-step process.

Received 16th October 2018,  
Accepted 21st December 2018

DOI: 10.1039/c8nr08375d

rs.c.li/nanoscale

### Introduction

Nanostructured materials (NMs) and nanoparticles (NPs)<sup>1</sup> are active areas of research of a burgeoning expansion in many techno-economic sectors and application domains, ranging from sensing and catalysis to healthcare. A considerable body

of work has been devoted to investigate the peculiar physicochemical characteristics of NPs, such as high surface-to-volume ratio, low melting point, curvature radius,<sup>2</sup> optical<sup>3</sup> and mechanical<sup>4,5</sup> responses toward their interactions with bacteria and cells in solution.<sup>6–8</sup> However, worldwide threats, like cross-contamination through infected surfaces in nosocomial environments<sup>9,10</sup> or biofilm formation on medical devices and implants,<sup>11</sup> necessitate biofouling and biocontamination prevention. This calls for a nanostructured coating with functionalities like antifouling<sup>12</sup> or bacterial release<sup>13</sup> actions. In particular, a bactericidal surface should be able to kill both Gram-positive and Gram-negative strains of multi-drug resistant pathogens. This state of things requires the development of functional nanostructured coatings capable of hindering the spread of a wide variety of different bacteria on solid surfaces by employing an effective eco-friendly synthesis technique with high throughput, thereby expanding the current research efforts beyond those involving microbicidal NPs in solutions.<sup>14–16</sup>

The key parameters influencing the coating/bacterial interactions and potential harmfulness against eukaryotic cells<sup>17</sup> are the NPs composition,<sup>18–20</sup> chemical state,<sup>14,15,21,22</sup> film morphology,<sup>18,23</sup> film porosity and root-mean-square (RMS) nano-roughness.<sup>24–26</sup> The challenge to go beyond a narrow-spectrum bactericidal coating, *e.g.*, composed of pure Ag NPs,<sup>27</sup> is to mix different microbicidal materials to form multi-elemental NPs. Among the potential microbicidal elements

<sup>a</sup>Interdisciplinary Laboratories for Advanced Materials Physics (i-LAMP) and Dipartimento di Matematica e Fisica, Università Cattolica del Sacro Cuore, Via Musei 41, 25121 Brescia, Italy. E-mail: luca.gavioli@unicatt

<sup>b</sup>Laboratory of Solid State Physics and Magnetism, Department of Physics and Astronomy, KU Leuven, Celestijnenlaan 200D, 3001 Leuven, Belgium

<sup>c</sup>Electron Microscopy Facility, Istituto Italiano di Tecnologia (IIT), Via Morego 30, 16163 Genova, Italy

<sup>d</sup>Dipartimento di Fisica, Università di Genova, Via Dodecaneso 33, 16146 Genova, Italy

<sup>e</sup>Institute for Nuclear and Radiation Physics, Department of Physics and Astronomy, KU Leuven, Celestijnenlaan 200D, 3001 Leuven, Belgium

<sup>f</sup>Department of Medical Biotechnologies, University of Siena, Viale Bracci 1, 53100 Siena, Italy

<sup>g</sup>Dipartimento di Medicina Sperimentale e Clinica, Università di Firenze, Largo Brambilla 1, 50134 Firenze, Italy

<sup>h</sup>Molecular Imaging and Photonics, Department of Chemistry, KU Leuven, Celestijnenlaan 200F, 3001 Leuven, Belgium

<sup>i</sup>FemtoNanoOptics group, Université de Lyon, Institut Lumière Matière (iLM), Université Lyon 1 and CNRS, 10 rue Ada Byron, 69622 Villeurbanne, France

†Electronic supplementary information (ESI) available: SCBD source functioning, NP size analysis, HR-TEM and EDX details, RBS measurements, XPS analysis, porosity estimation, MD simulation results, human cytotoxicity results. See DOI: 10.1039/c8nr08375d

(Ag, Al, Cu, Mg, Ni, Ti, and Zn<sup>14–16,21,28</sup>), the remarkable activity of Ag against Gram-negative bacteria<sup>27</sup> and that of Cu against Gram-positive bacteria and yeasts<sup>15,28</sup> intuitively suggest the combination of these two elements as extremely promising.<sup>29,30</sup> In addition, we recently showed that adding elements with greater oxygen chemical affinity<sup>31</sup> to metallic NPs considerably enhances the nanostructured film adhesion to the substrate,<sup>18</sup> Mg being a potentially viable candidate for this scope. A multielemental NP film combining Mg, Ag, and Cu, therefore, seems a promising coating, potentially capable of fulfilling all the above mentioned requirements.

The bactericidal efficiency of a coating could be further increased if we can synthesize a nanostructured material with a high surface-to-volume ratio, controlled morphology and thickness, wherein multielemental NPs preserve their composition and properties. However, this process has, so far, been marred by several issues. For instance, the coating synthesis by wet routes is hampered by problems related to colloidal stabilization, substrate functionalization, solvent purification and other multistep processes,<sup>32</sup> while non-wet synthesis routes<sup>25,33–36</sup> have, so far, not been able to achieve such goals either with regard to optimal size and composition of NPs or with respect to the coating thickness, roughness and morphology control. A promising alternative solution for the synthesis of a green and affordable multielemental NP coating is the supersonic cluster beam deposition (SCBD) technique.<sup>18</sup> This eco-friendly method is based on the gas-phase synthesis of directly deposited NPs forming homogeneous films<sup>4,5,27</sup> with controllable morphology parameters<sup>24,26,37</sup> on a wide variety of substrates.

The open challenge is, therefore, to combine Mg, a biocompatible element improving the coating adhesion/mechanical stability,<sup>38</sup> with the bactericidal elements (Cu and Ag) in NPs, followed by assembling these NPs into a nanostructured coating by employing an effective eco-friendly synthesis technique with high throughput. More specifically, from the materials science point of view, the elemental NP composition has to be addressed. For instance, the atomic distribution of a multielemental NP combining Mg, Ag, and Cu could be largely different with respect to a simpler case where common Ag<sub>core</sub>-Cu<sub>shell</sub> NPs are synthesized in the absence of Mg.<sup>39,40</sup> From the microbiological viewpoint, the envisioned wide-spectrum microbicidal activity may be affected by the final element chemical state, NPs distribution and coating morphology, or eventual materials cooperative effects, the actual efficacy still remains to be determined.

In this work, we engineer a nanostructured coating by bottom-up assembly of Janus-like NPs with tunable composition and with unprecedented bactericidal spectrum. The link between the physicochemical properties of the granular coating and its bactericidal effect is addressed. We use X-ray photoemission spectroscopy (XPS) to characterize the NPs' chemical states and Rutherford backscattering spectrometry (RBS) to quantify the film's elemental stoichiometry and porosity. The RMS roughness of the coating,<sup>24</sup> influencing the bacterial adhesion to the substrate, is investigated by atomic force

microscopy (AFM). High-resolution transmission electron microscopy (HR-TEM) and high-angle annular dark-field scanning transmission electron microscopy (HAADF-STEM), combined with energy dispersive X-ray spectroscopy (EDX), reveal the Janus-like NPs morphology, partly exposing the bactericidal clusters of metallic Cu and Ag to the environment. Molecular dynamic (MD) simulations show that MgO plays the cardinal role in the formation of clusters with a partial Ag<sub>core</sub>-Cu<sub>shell</sub> structure, while the effective wide-spectrum antimicrobial activity is proven on *Escherichia coli* ATCC 25922 and *Staphylococcus aureus* ATCC 6538 reference strains. Furthermore, viability tests on two human cell lines (HeLa and A549) after 24 h of direct exposure to the tri-elemental NPs have been performed to quantify the cytotoxicity of the bactericidal film.

## Results and discussion

### Morphology of NPs

The elemental distribution inside the NPs is of paramount importance for both bactericidal activity and mechanical properties of the bottom-up-assembled NM. Small metallic clusters are desirable to create ultra-active bactericidal hot spots, as shown for Pd-W<sup>23</sup> and Ag-Ti<sup>18</sup> bi-elemental NPs. Furthermore, previous works have shown that the presence of a metal oxide matrix partly embedding Ag hot spots allowed to increase the mechanical stability of NPs, creating a nanostructured coating that could strongly adhere to plastic and glass substrates.<sup>18</sup>

Fig. 1a and b show two HAADF-STEM images of scattered AgCuMg202060 and AgCuMg503020 NPs, respectively, deposited onto a carbon-coated Au TEM grid. Because of the atomic number sensitivity of this imaging technique, regions

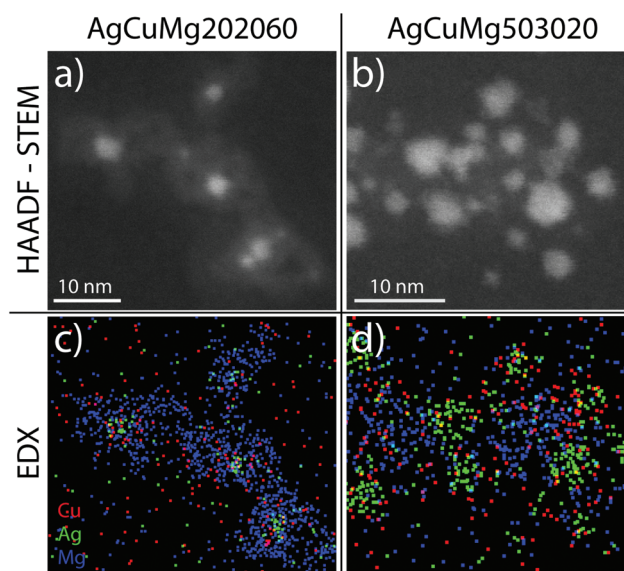


**Fig. 1** HAADF-STEM (top panels) and corresponding EDX elemental maps (bottom panels). Cu (red), Ag (green), and Mg (blue) for the AgCuMg202060 (a, c) and AgCuMg503020 (b, d) NP samples.

with different contrasts are observable in this image; therefore, they can be associated to the position of different elements. The brightest areas (average diameter:  $1.8 \pm 0.8$  nm for AgCuMg202060 and  $3.0 \pm 1.7$  nm for AgCuMg503020; see the histograms plotted in Fig. S2 of the ESI† for more details) can be ascribed to NPs containing heavier elements such as Ag and Cu, whereas the less bright zones are likely to be related to Mg. This contrast-based observation is confirmed by the EDX maps presented in Fig. 1c and d, showing that for both AgCuMg202060 and AgCuMg503020, Ag (green) and Cu (red) are mostly concentrated in the brighter areas, while Mg (blue) is distributed in the surrounding. Hence, one can deduce that the synthesized NPs assume a cluster-in-cluster (Janus) form, with a Mg-rich matrix partially embedding Ag and Cu clusters. The rather low signal-to-background ratio in the EDX maps (also refer to the corresponding EDX spectra shown in Fig. S3 of ESI†) does not allow to distinctly visualize whether the Ag-Cu clusters are alloyed or phase-segregated. Considering the immiscible nature of Ag and Cu,<sup>41</sup> the most likely scenario is the segregation of these two elements instead of an alloyed arrangement. HR-TEM analyses, performed on both the samples, clearly reveal crystalline Ag NPs, the largest ones exhibiting a typical multi-twinned structure (see Fig. S4 of ESI†). On the other hand, tiny MgO crystals were found in the AgCuMg202060 NP sample, while no clearly ordered structures were detected within the Mg-poor samples. No crystalline particles ascribable to Cu, or oxidized Cu, were identified by HRTEM, probably due to the small size of Cu domains, which did not allow for the formation of periodic structures. Further investigations on their structures have been carried out by using MD simulations, described further in this manuscript.

For applications as a microbicidal coating, the most promising candidate is AgCuMg503020 since the higher relative abundance of Mg inside AgCuMg202060 NPs almost completely impedes the exposure of Ag and Cu clusters. Indeed, a weight concentration of Ag/Cu/Mg 20/20/60% is equivalent to an atomic concentration of 6/11/83%, resulting in a very low presence of Ag and Cu inside the coating. As such, we focused on the AgCuMg503020 for performing a comprehensive investigation.

### Relative elemental composition of NPs

Tailoring NMs with the desired relative elemental composition is crucial to synthesize *ad hoc* bactericidal coatings having specific physical and biological properties, such as cytotoxicity or adhesion to the substrate.<sup>3,18</sup> We employ RBS to relate the actual NP composition with the nominal one of the starting target rod—a macroscopic parameter—to prove the effective tunability of the film constituents and exploit the SCBD flexibility. RBS was obtained from an  $85 \pm 5$  nm-thick film of AgCuMg503020 deposited on HOPG (the thickness was measured by AFM at the film edge, see Fig. S6†). The choice of a light element (C) substrate allows to precisely quantify all the elements heavier than carbon. The data, visible in sections 3 and 5 of the ESI,† show that the relative weight content of the NPs (Ag/Cu/Mg = 47/29/24) is compatible with the nominal one of the starting rod (50/30/20), indicating a direct transfer

of all the elements from the macroscopic rod to the nanostructured film. This direct correspondence demonstrates, for the first time, the possibility of fine-tuning the elemental composition of tri- and multielemental NPs by using a SCBD source. A more detailed quantification of the NP film contents (including O) is reported in the ESI† (sections 3 and 5).

### Chemical state

Since the chemical states of Ag, Cu, and Mg strongly influence their bactericidal activity,<sup>14,21,29</sup> a thorough XPS analysis was carried out on a 20 nm-thick film of AgCuMg503020 deposited on Ta. The data show that Ag and Cu are metallic, while Mg forms oxides. Considering the antibacterial activity of metallic Ag,<sup>18</sup> MgO,<sup>42</sup> and Mg(OH)<sub>2</sub><sup>43</sup> against a wide number of Gram-negative bacteria and of metallic Cu against many Gram-positive bacteria,<sup>6,29</sup> the present chemical composition of the NPs is a promising candidate to create a wide-spectrum bactericidal NM.

The main XPS core-level peaks (Ag 3d, Cu 2p, C 1s, O 1s, Mg 1s, and Mg 2p) are shown in Fig. 2, together with the fits of the different components. The binding energy (BE) positions and intensities of all the peaks are listed in Table 1 for future reference. The BE and spin-orbit splitting energy of Ag 3d peaks (Fig. 2a) confirm the metallic form of Ag, similar to that recently found on NPs synthesized with pure Ag and Ag-Ti *via* SCBD.<sup>5,18</sup>

The Cu 2p line shape (Fig. 2b) is characterized by the presence of two main photoemission structures at 932.8 and 952.7 eV BE, which is compatible with the peak positions of metallic Cu,<sup>44</sup> and of the two minor peaks at 934.6 and 956.2 eV BE, which could be ascribed to CuO.<sup>45</sup> The relative areas of these two peaks are less than 10% of the total area of the main Cu features. Moreover, the data reveal only a small shake-up structure around 945 eV BE, which was also observed in metallic Cu.<sup>44</sup> These results, therefore, indicate that the Cu inside the NPs is also mostly metallic, even though a limited interaction with the oxygen of the surrounding shell might occur.<sup>44</sup>

Both Mg 2p and Mg 1s spectra (Fig. 2e and f) reveal a single, broad peak resulting from the superposition of different components. Then, the analysis of these photoemission lines, assuming that three possible stable Mg chemical states are separately contributing to the Mg line shape (MgO, Mg(OH)<sub>2</sub>, and MgCO<sub>3</sub>), has to be supported by the simultaneous analysis of the C 1s and O 1s peaks (Fig. 2c and d, respectively). The detailed analysis, reported in the ESI† (section 4), reveals that the relative concentrations of MgO, Mg(OH)<sub>2</sub>, and MgCO<sub>3</sub> are 42%, 39%, and 19%, respectively.

The metallic state of Ag and Cu can be explained considering the chemical affinity with oxygen of the elements comprising the NPs. The metallic states of Ag and Cu can be explained considering their chemical affinity with oxygen (*i.e.*, the negative partial derivative of the Gibbs energy,  $G$ , with respect to the extent of the reaction,  $\xi$ ),

$$\Delta Z = -\frac{\partial G}{\partial \xi}$$

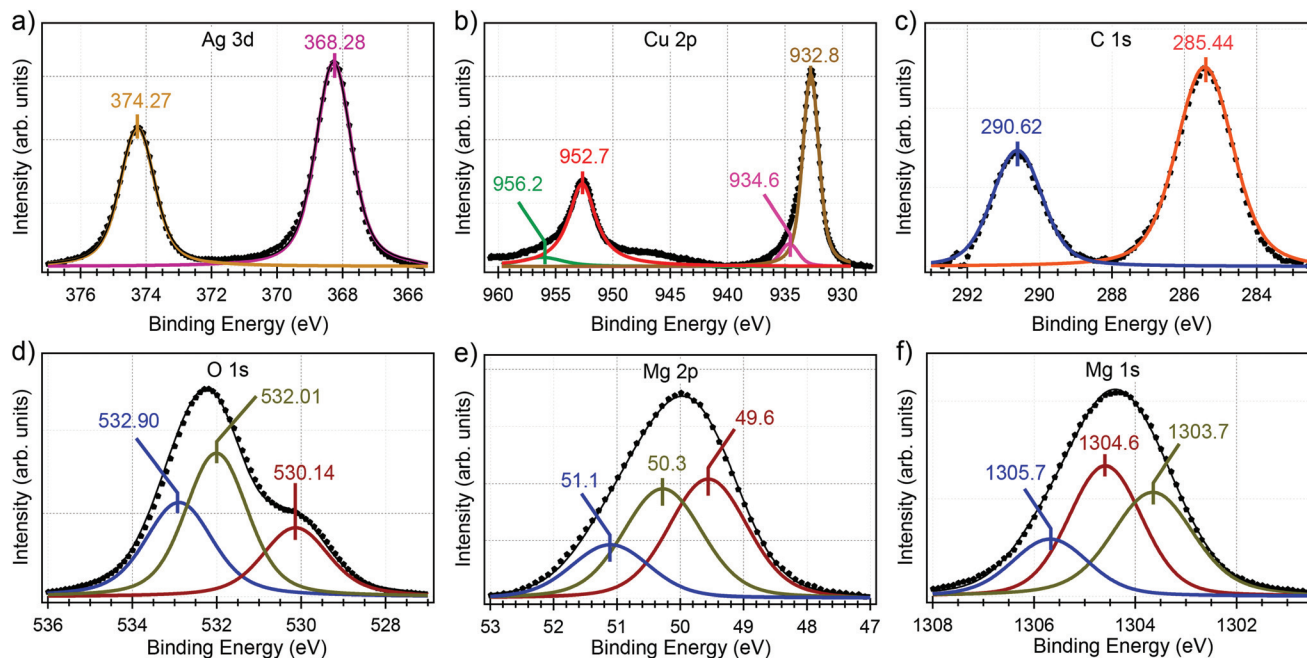


Fig. 2 XPS Ag 3d (a), Cu 2p (b), C 1s (c), O 1s (d), Mg 2p (e), and Mg 1s (f) spectra of a AgCuMg503020 NP thin film. Dark red fits refer to MgO; green fits, Mg(OH)<sub>2</sub>; and blue fits, MgCO<sub>3</sub>. Solid black lines indicate the sum of the fitting Voigt functions, and black markers indicate the experimental data.

**Table 1** XPS results of core-level peaks obtained in this work for all the materials under investigation. BE, FWHM, and relative area with respect to the total area of the peaks for Ag, Cu, C, O, and Mg. BE errors are estimated by considering the largest BE variation of the peak center, resulting from changes in the background subtraction and fitting parameters. The last column indicates the chemical state of the element generating the peak

Peak	BE (eV)	FWHM (eV)	Relative A	Source	
Ag	3d <sub>3/2</sub>	374.27 ± 0.04	1.07	40%	Metallic Ag
	3d <sub>5/2</sub>	368.28 ± 0.04	1.11	60%	Metallic Ag
Cu	2p <sub>1/2</sub>	956.2 ± 0.1	4.01	6%	CuO
	2p <sub>1/2</sub>	952.7 ± 0.1	2.86	42%	Metallic Cu
	2p <sub>3/2</sub>	934.6 ± 0.1	1.86	6%	CuO
	2p <sub>3/2</sub>	932.8 ± 0.1	1.65	46%	Metallic Cu
C	1s	290.62 ± 0.05	1.44	—	MgCO <sub>3</sub>
O	1s	530.14 ± 0.05	1.64	24%	MgO
	1s	532.01 ± 0.05	1.53	44%	Mg(OH) <sub>2</sub>
	1s	532.88 ± 0.05	1.67	32%	MgCO <sub>3</sub>
Mg	2p	49.56 ± 0.10	1.33	42%	MgO
	2p	50.28 ± 0.10	1.33	39%	Mg(OH) <sub>2</sub>
	2p	51.11 ± 0.10	1.32	19%	MgCO <sub>3</sub>
	1s	1304.6 ± 0.1	1.56	42%	MgO
	1s	1303.7 ± 0.1	1.66	39%	Mg(OH) <sub>2</sub>
	1s	1305.7 ± 0.1	1.59	19%	MgCO <sub>3</sub>

for the elements comprising the NPs:<sup>31</sup>

$$\Delta Z \left( \text{Cu} + \frac{1}{4} \text{O}_2 \rightarrow \frac{1}{2} \text{Cu}_2\text{O} \right) = 73 \text{ kJ mol}^{-1},$$

$$\Delta Z \left( \text{Cu} + \frac{1}{2} \text{O}_2 \rightarrow \text{CuO} \right) = 128 \text{ kJ mol}^{-1},$$

$$\Delta Z \left( \text{Ag} + \frac{1}{4} \text{O}_2 \rightarrow \frac{1}{2} \text{Ag}_2\text{O} \right) = 5.5 \text{ kJ mol}^{-1},$$

$$\Delta Z \left( \text{Mg} + \frac{1}{2} \text{O}_2 \rightarrow \text{MgO} \right) = 564 \text{ kJ mol}^{-1}.$$

These values explain why, in the presence of oxygen, metallic Mg tends to quickly and spontaneously oxidize in the NPs, while Ag and Cu remain metallic.

### Topography and porosity

The surface nano-roughness has been shown to influence the bacterial<sup>24,46</sup> and cellular<sup>26,46</sup> adhesion, and consequently, the biofilm formation<sup>47</sup> and bactericidal effect. In particular, RMS roughness higher than 20 nm is shown to decrease the bacterial-surficial interaction, whereas a small roughness value increases this interaction.<sup>24</sup> Depending on the specific application, the NP density on the substrate and the thickness of the antibacterial coating synthesized by SCBD can be tailored in a wide range, starting from isolated NPs with a totally covered surface area of 1% to a single monolayer film up to hundreds of nanometers thick. Fig. 3a shows the representative 4 μm × 4 μm 3D AFM image of the surface morphology of an 85 nm-thick film of AgCuMg503020 NPs deposited onto a silicon substrate. The image is characterized by the presence of NPs with spatially uniform distribution, inducing granular morphology in the coating. This behavior is a

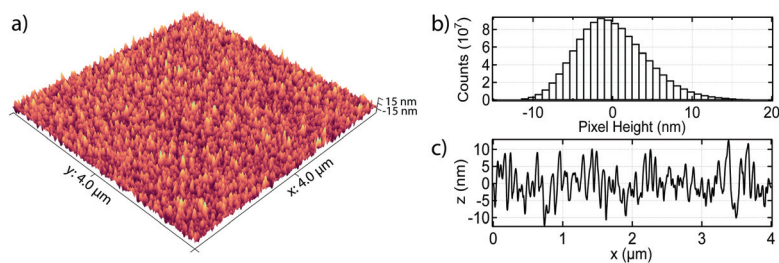


**Fig. 3** (a) Topographic 3D view of the AFM image of an 80 nm-thick AgCuMg503020 NP sample deposited onto flat Si. (b) Pixel height distribution of the entire image. (c) Representative line scan taken from (a).

common feature of films obtained *via* SCBD, independently from the substrate and from the material comprising the NPs, due to the soft-landing regime ruled by the synthesis conditions.<sup>4</sup> The pixel height distribution, obtained after third-order polynomial background subtraction, is shown in Fig. 3b along with a representative line scan (Fig. 3c). The RMS roughness (obtained from the pixel height distribution of several topographic images obtained from different film areas) is  $4.5 \pm 0.2$  nm, which is similar to the values obtained for films of Ag<sup>27</sup> and Ti<sup>48</sup> NPs deposited in similar synthesis conditions and substrates. Such a small roughness value is expected to facilitate interactions between the bacteria and bactericidal coating, allowing the full exploitation of the film's killing activity.

Considering the granular nature of the film, the most likely scenario is that the film comprises solid NPs with small voids and channels between them, such as that in pure Ag NPs.<sup>4,49</sup> RBS was used on this thick film to directly quantify the number of atoms per unit area for each constituent and, consequently, to estimate the film porosity. The expected thickness of a nonporous film with the RBS-measured number of atoms per unit area is 68 nm. Since the actual AFM-measured film thickness is  $85 \pm 5$  nm, the obtained film porosity is  $20 \pm 4\%$ ; the error is induced by the uncertainty of the AFM-estimated film thickness. This value is similar to those already obtained for Ag NP films ( $20 \pm 6\%$ )<sup>4,5</sup> and Ag-Ti NP films ( $25 \pm 5\%$ )<sup>3</sup> with the same synthesis apparatus. Further details are reported in the ESI† (section 5). The present results indicate that the SCBD synthesis method yields NPs and coatings with remarkably similar surface morphology and porosity, even when the number of elements comprising the NP is larger than two. The present results suggest that the granular NP film morphology is primarily related to the NP formation process (size) and gas dynamics (kinetic energy/atom) as opposed to the specific chemical species (*i.e.*, interatomic potential) involved.

### MD simulations

To gain an insight into the dynamics of the physical processes leading to NP formation and to rationalize the distribution of elements inside each NP, we used MD simulations. MD is emerging as the go-to technique for mechanical and thermal nanometrology,<sup>50</sup> complementing finite elements

method-based<sup>51</sup> or other *ab initio* approaches.<sup>52</sup> During NP formation, the quantity of available impurities inside the ablation chamber is insufficient to produce stoichiometric magnesium oxides, hydroxides, and carbonates. Since there is no structural information on NP coalescence inside the ablation chamber, it is not possible to develop a first-principles model of the Mg-metal interface. Therefore, we employed a semi-empirical model of the interaction between Ag/Cu and the (100) surface of MgO. Assuming the NPs completely coalesced in the ablation chamber, thereby keeping MgO as the outer shell, in order to replicate the embedding of metal clusters in the Mg matrix, we performed the MD simulation of a cubic cavity of MgO (size:  $2 \times 2 \times 2$  nm<sup>3</sup>). At full loading, the cavity can contain approximately 350 metal atoms. The size of the metal cluster is, consequently, similar to the metallic inclusion size shown in Fig. 1b, which allows for a comparison with the experimental results and, at the same time, is computationally feasible.

Our simulations started from a configuration with the metal Ag/Cu mixture (40/60 at% corresponding to the experimental concentration in NPs) in the liquid state. Successively, the temperature of the system was gradually decreased from 800 K to 400 K. The liquid-to-solid transition of the metal (Fig. S7†) is located at 650 K. In our simulations, we monitored the composition of the metal layer at the interface with the MgO surface. We calculated the relative number of MgO-Cu and MgO-Ag contacts as a function of temperature during the cooling process. In the liquid phase, the fraction of MgO-Cu contacts with respect to the total MgO-metal contacts is larger than 0.6, indicating that Cu prefers occupying sites at the interface with MgO (Fig. S8 and S9†). The situation does not change when the cluster solidifies. The transition to the solid state implies an increase in phase segregation, as quantified by the decrease in Ag-Cu contacts (shown in Fig. S8 and S9†). The structure revealed by the MD simulations, characterized by a Ag core partially surrounded by smaller phase-segregated Cu aggregates lying at the interface with the MgO matrix, is evident in Fig. 4 and Fig. S10† and is compatible with the EDX maps shown in Fig. 1d. It should be noted that usually, Ag-Cu NPs in the gas phase are expected to exhibit very strong phase segregation, resulting in the formation of Cu<sub>core</sub>-Ag<sub>shell</sub> clusters.<sup>39,40</sup> Here, the MgO surface reverses the cluster chemical ordering, driving Cu to the oxide interface. Even though the observed partial Ag<sub>core</sub>-Cu<sub>shell</sub> structure allows the exposure of

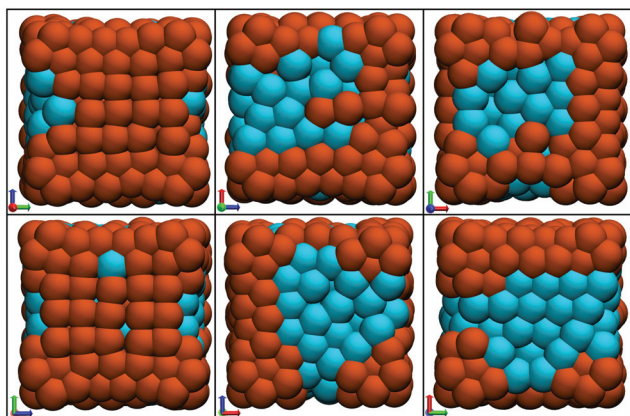


Fig. 4 Rendering of the final atomic distribution at 400 K obtained from the MD simulations. Orange spheres represent Cu atoms; light-blue spheres, Ag atoms; MgO, not visible. The results indicate an incomplete  $\text{Ag}_{\text{core}}-\text{Cu}_{\text{shell}}$  structure of the clusters.

all the elements contained in the coating, the tendency of Cu to occupy the outer sites could increase the effective exposed area of Cu with respect to Ag and the consequent bactericidal effect.

### Bactericidal effect

The antibacterial activity of multielemental NP coatings was tested against both Gram-negative and Gram-positive reference strains (*E. coli* ATCC 25922 and *S. aureus* ATCC 6538, respectively). We individually deposited a thin layer of AgCuMg503020 NPs and that of pure Mg NPs on soda-lime glass substrates, with an average thickness of 6 nm for both the compositions. This thickness corresponds to a single monolayer of NPs. Each sample has been contaminated with a standardized bacterial suspension of about  $1 \times 10^7$  colony-forming unit (CFU)  $\text{mL}^{-1}$  and incubated at 25 °C in a dark and damp environment for 3 h. The subsequent measurements of the viable bacterial count on the AgCuMg503020-NP-coated substrate, as shown in Fig. 5, show a decrease of more than 4 orders of magnitude of viable cells for both Gram-negative and Gram-positive bacteria, indicating a relevant bactericidal effect. If compared to pure Ag<sup>27</sup> and AgTi<sup>18</sup> NPs obtained under similar synthesis conditions, where Gram-positive bacteria were almost unaffected by the NP action after 3 h, the present tri-elemental NPs provide an outstanding bactericidal activity against *S. aureus*, confirming the wider-spectrum activity of this coating.

In order to verify whether the bactericidal activity of the AgCuMg503020 NP coating might be related to Mg, the same tests were repeated on a single layer of Mg NPs on glass (Mg). No substantial decrease in viable bacteria was observed after 3 h of exposure (Fig. 5), indicating that, in this context, Mg is harmless to the tested strains and that the remarkable bactericidal effect of the AgCuMg503020 films can be related to the metallic components of NPs. The cause of the bactericidal effect, either due to Cu alone or the cooperative and synergistic effects of both Ag and Cu, as reported in the case of other

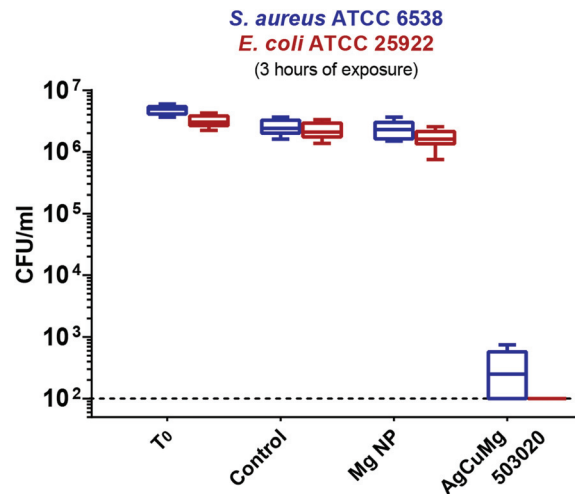


Fig. 5 Box-and-whisker plots showing the results of microbicidal tests on *S. aureus* (blue) and *E. coli* (red). Each plot is a comparison between the count of viable bacteria (reported as CFU per milliliter) of the control before incubation ( $T_0$ ), control bare substrate after incubation (Control), pure Mg NP film (Mg NP), and wide-spectrum tri-elemental AgCuMg503020 NPs. The dashed line at  $10^2$  CFU  $\text{mL}^{-1}$  is the limit of detection of the experiment.

nanocomposites,<sup>20,22</sup> is yet to be determined. Putting things into perspective, a deeper understanding of the mechanism of action in damaging the cytoplasmic membrane of bacterial cells will require the determination of the metal-ion-releasing properties of this composite coating.

The proposed solution represents the first SCBD-synthesized wide-spectrum bactericidal NM effectively able to hinder the spread of both Gram-positive and Gram-negative pathogens on contaminated surfaces.

### Human toxicity

Viability tests on HeLa and A549 cells were performed to evaluate the cytotoxicity of the nanocomposite bactericidal coating toward human cells. Bright-field images of HeLa and A549 cells after 24 h of incubation show that the cell viability was minimized upon direct contact with NPs as compared to the controls (Fig. S11†). This was further confirmed from the corresponding viability tests (Fig. S11e†), which revealed that after 24 h of incubation with NPs, the cell viability, expressed as the mean percentage of viable cells related to the control ( $\pm$  standard deviation) was  $8 \pm 5\%$  and  $13 \pm 12\%$  for HeLa and A549 cells, respectively. Since Mg is considered to be a biocompatible element<sup>38</sup> and Au NPs are harmful only upon cellular uptake<sup>53,54</sup> (very unlikely in the case of a thin film of NPs strongly bound to the substrate), the marked toxicity of the NPs toward human cells could be mainly associated to Cu.<sup>17</sup> Considering that the bactericidal activity is taking place within 3 h, and possibly faster, the applications of such coatings should take into account the time scale of the bactericidal response. In the case of future specific applications, where a direct contact with human cells is needed (e.g., prosthesis or

dental implants), additional experimental data on the cytotoxicity effects toward animal living cells are required. Such prospective work could allow obtaining a balance between bactericidal activity and cytotoxic effects by synthesizing an *ad hoc* tuned NP with decreased Cu content. Given the direct correspondence of the NP content with the target rod demonstrated above, for the synthesis of safer NMs, it will suffice to decrease the amount of Cu in the ablated material (e.g., AgCuMg502030).

## Experimental

### NP synthesis

Multielemental NPs were synthesized by the SCBD setup, which exploits pulsed high-pressure He injection in a low-vacuum ( $10^{-2}$  mbar) chamber and synchronized discharge to ignite a plasma that homogeneously erodes all the constituents of the target rod. The quenched atoms consequently condense into NPs and are extracted through an aerodynamic system, forming a beam directed toward the substrate. The starting materials, which were used as ablation targets, were sintered rods composed of Ag, Cu, and Mg at nominal concentrations of 20/20/60 wt% (AgCuMg202060) and 50/30/20 wt% (AgCuMg503020). To understand the specific role of Mg in the bactericidal test, Mg NPs were also synthesized starting from a pure Mg rod. Additional details on the synthesis setup can be found in the ESI† (section 1) or elsewhere.<sup>18</sup>

### TEM

HR-TEM and HAADF-STEM imaging and EDX analysis were carried out by an image-Cs-corrected JEOL JEM-2200FS microscope, with a Schottky source (operated at 200 kV), equipped with a Bruker XFlash 5060 EDX system. For these analyses, the samples were prepared by SCBD deposition directly onto a Au grid, coated with a double amorphous carbon layer (ultrathin carbon on holey carbon). An analytical sample holder was used with the aim of minimizing spurious contributions to the EDX spectra (particularly for Cu as we needed to map and quantify this element). Elemental maps for Mg, Ag, and Cu were obtained by integrating the Mg-K, Ag-L $\alpha$ , and Cu-K $\alpha$  peaks in the EDX spectrum, respectively, within the analyzed area.

### XPS

XPS data were collected in an Omicron MultiScan Lab UHV apparatus (base pressure lower than  $2 \times 10^{-10}$  mbar) equipped with a SPECS Phoibos 100 hemispherical electron energy analyzer and a standard X-ray source (Al-K $\alpha$  line). The XPS data were acquired with the analyzer normal to the sample surface at fixed analyzer transmission in the small-area mode with pass energy of 20 eV. The BE values were determined by measuring the Fermi edge of a Au reference substrate in contact with the samples. A Shirley-like background was removed from all the XPS spectra. A least-square fitting procedure using Voigt functions was used to determine the inten-

sity and energy position of the structures. No charging of the sample was observed during the XPS analysis. XPS quantification was performed by using the areas of each peak divided by the atomic sensitivity factor<sup>44</sup> and corrected with the energy-dependent inelastic mean free path (IMFP) of the electrons for MgO.<sup>55</sup> The sample for XPS analysis was created by coating a polycrystalline Ta film, previously treated with ozone for 2 h, with a 20 nm-thick film of AgCuMg503020 NPs.

### AFM

AFM (Solver pro NT MDT) was operated in the tapping mode using an Etalon HA-NC tip with a nominal radius of 10 nm.

### RBS

RBS measurements were performed using 1.57 MeV He<sup>+</sup> ions impinging on the sample at an angle of 5° with respect to the sample normal. Two detectors were simultaneously used, positioned to obtain scattering angles of the detected particles of 167° and 105.5°. The ratio of the constituents (and hence, the composition of the layer) was directly derived from the Rutherford equation, whereas the areal density was calculated using the standard Ziegler–Biersack–Littmark (ZBL) stopping power values.

### MD Simulations

To setup the MD simulations, a homemade package was used. The analyzed system consisted of 345 atoms with a composition of Ag:Cu—40:60 entrapped in a MgO box of  $2 \times 2 \times 2$  nm<sup>3</sup> to reproduce the relative Ag:Cu composition of AgCuMg202060 NPs. The volume of the box was fixed during the simulation and the MD runs were performed in a canonical ensemble with the temperature maintained constant by an Andersen thermostat. The time step of the simulation was 0.005 fs, and the state of the system was saved every 0.25 ns. Two independent initial configurations were extracted from an equilibration run at 2000 K (in which the metal is in the liquid state), cooled down to 800 K, and further equilibrated for 50 ns in the liquid state. Starting from 800 K, the system was slowly cooled down, at a rate of 0.1 K ns<sup>-1</sup>, until the temperature of 400 K was reached. A semi-empirical potential to describe the interaction between Ag/Cu and the (100) surface of MgO was used, as developed by Vervisch *et al.*<sup>56</sup> This model was previously used to study the structure of Ag<sup>57</sup> and Ag–Cu<sup>58</sup> clusters on MgO. With regard to the metal–metal interactions, an empirical atomistic forcefield derived within the second-moment approximation to the tight-binding model (SMATB potential) was used.<sup>57,58</sup>

### Contacts analysis

The contact analysis determines how many atoms of each species are either the nearest neighbor of each other or in contact with the MgO walls. The number of contacts between the metal atoms (Ag–Ag, Ag–Cu, and Cu–Cu) was obtained using a homemade tool with threshold contact distance of 0.30 nm. Then, the number of contacts was averaged every 2.5 ns. With regard to the number of contacts between MgO and

metals (MgO–Ag and MgO–Cu), a contact was recorded if the distance perpendicular to the MgO plane and the metal was less than 0.32 nm; then, the number of contacts was normalized by the total number of contacts of the MgO.

### Antibacterial activity

Bactericidal tests were performed with the reference strains of *E. coli* ATCC 25922 and *S. aureus* ATCC 6538 on soda-lime-glass 20 × 20 mm<sup>2</sup> cover slips (Menzel–Glaser). Each support was placed in a 6-well polystyrene tissue culture plate (IWAKI microplate, Bibby Scientific Limited, Staffordshire, UK), contaminated with a standardized bacterial suspension (*i.e.*, about 1 × 10<sup>7</sup> CFU mL<sup>-1</sup> in phosphate buffered saline, PBS; pH 7.3) and incubated at 25 °C in a dark and damp environment for 3 h. After the incubation time, the bacterial cells were removed from the supports by adding 2 ml of PBS containing 1% Tween-20 (a surfactant favoring the detachment of bacteria from the supports), incubating for 30 min, and gently pipetting. Appropriate dilutions (*i.e.*, 80 µl for each 10-fold dilution) were successively plated onto tryptic soy agar (TSA) (Oxoid, Milan, Italy) for obtaining a viable cell count. Soda-lime-glass cover slips without NP films were treated in the same way and used as controls. All the data were obtained in two independent experiments, with three replicates per condition per experiment.

### Human cytotoxicity

HeLa and A549 cells were maintained in a DMEM medium containing 10% FBS, 1% L-glutamax, and 0.1% gentamicin and cultured in 25 cm<sup>2</sup> cell culture flasks at 37 °C and under a humidified 5% CO<sub>2</sub> atmosphere. The cell passage was performed *via* trypsinization every 2–3 days, when the confluency reached 80%. To perform the viability tests, the cells were seeded in a TC Dish 35 standard dish (SARSTEDT), which was precoated with a monolayer of AgCuMg503020 NPs (average thickness: 6 nm). After 24 h of incubation at 37 °C under humidified 5% CO<sub>2</sub> atmosphere, the cell viability was estimated by comparing the number of viable cells in the NP-coated dishes with the number of viable cells in the control bare dishes. Cell counting was performed by trypsinizing the cells and depositing aliquots of the cell suspension in a Glasstic slide 10 with grids (KOVA). The estimation of a viable cell number was accomplished by following the KOVA system protocol; nonviable cells were stained with trypan blue solution so that they could be excluded from the counting process. The viability data were expressed as a mean percentage of the viable cells as compared to the control.

## Conclusions

Here, a new family of NP-based bactericidal coatings composed of Ag, Cu and Mg and synthesized by a green gas-phase technique was proposed. These coatings are effective against both Gram-positive and Gram-negative reference strains. SCBD allows the synthesis of tri-elemental NPs with tunable relative

concentration of the elements. The NPs are characterized by phase-segregated incomplete core–shell clusters of metallic Ag<sub>core</sub>–Cu<sub>shell</sub>, partially embedded in a MgO matrix. This structure is replicated into the coatings, forming a granular film with RMS roughness below 5 nm and porosity of 20 ± 4%. Granular coatings exhibit wide-spectrum bactericidal activity because of the exposure of Ag and Cu metallic clusters to the environment due to the low film roughness. The remarkable bactericidal activity of the coating, together with the possibility to fine tune the NP composition by exploiting the SCBD flexibility, represent a striking progress in the development of nanocomposite bactericidal coatings and an excellent opportunity for technological transfer to several healthcare-related applications.

The present results open up a wide spectrum of interesting research paths necessitating further work to be pursued in the near future to fully exploit the potential offered by multielemental NP films. For instance, the antimicrobial properties of Ag–Cu–Mg NMs against a broader spectrum of microorganisms will have to be tested to establish its effectiveness against other microorganisms of medical interest, as well as microbicidal (as opposed to microbiostatic) activity. NP films can also be integrated with other technologies to enhance bactericidal activity. For instance, surface acoustic waves (SAW) could be launched in a photonic crystal, nanopatterned with NP films, so as to mechanically assist the bactericidal killing action.<sup>59</sup> The device scheme would rely on the photoacoustic excitation of SAW;<sup>51</sup> the photoacoustic transduction capabilities of similar NP scaffolds having already been proven.<sup>5,49</sup>

## Conflicts of interest

There are no conflicts to declare.

## Acknowledgements

G. B., A. V. and M. J. V. B. acknowledge financial support from the Research Foundation Flanders (FWO) and the KU Leuven Research Fund (GOA/14/007 and C14/18/074). L. G., and E. C. acknowledge support from Università Cattolica del Sacro Cuore through D.2.2 and D.3.1 grants.

## Notes and references

- 1 J. Jeevanandam, A. Barhoum, Y. S. Chan, A. Dufresne and M. K. Danquah, *Beilstein J. Nanotechnol.*, 2018, **9**, 1050–1074.
- 2 F. Baletto and R. Ferrando, *Rev. Mod. Phys.*, 2005, **77**, 371.
- 3 E. Cavaliere, G. Benetti, M. Van Bael, N. Winckelmans, S. Bals and L. Gavioli, *Nanomaterials*, 2017, **7**, 442.
- 4 G. Benetti, C. Caddeo, C. Melis, G. Ferrini, C. Giannetti, N. Winckelmans, S. Bals, M. J. Van Bael, E. Cavaliere, L. Gavioli and F. Banfi, *J. Phys. Chem. C*, 2017, **121**, 22434–22441.

- 5 S. Peli, E. Cavaliere, G. Benetti, M. Gandolfi, M. Chiodi, C. Cancellieri, C. Giannetti, G. Ferrini, L. Gavioli and F. Banfi, *J. Phys. Chem. C*, 2016, **120**, 4673–4681.
- 6 B. Khodashenas, *Indian Chem. Eng.*, 2016, **58**, 224–239.
- 7 M. Ul-Islam, A. Shehzad, S. Khan, W. A. Khattak, M. W. Ullah and J. K. Park, *J. Nanosci. Nanotechnol.*, 2014, **14**, 780–791.
- 8 K. S. Siddiqi, A. Husen and R. A. K. Rao, *J. Nanobiotechnol.*, 2018, **16**, 14.
- 9 E. I. Kritsotakis, F. Kontopidou, E. Astrinaki, M. Roubelaki, E. Ioannidou and A. Gikas, *Infect. Drug Resist.*, 2017, **10**, 317–328.
- 10 I. Wille, A. Mayr, P. Kreidl, C. Brühwasser, G. Hinterberger, A. Fritz, W. Posch, S. Fuchs, A. Obwegeser, D. Orth-Höller and C. Lass-Flörl, *J. Hosp. Infect.*, 2018, **98**, 90–95.
- 11 K. A. Floyd, A. R. Eberly and M. Hadjifrangiskou, in *Biofilms and Implantable Medical Devices*, ed. Y. Deng and W. Lv, Woodhead Publishing, 2017, pp. 47–95.
- 12 I. Banerjee, R. C. Pangule and R. S. Kane, *Adv. Mater.*, 2011, **23**, 690–718.
- 13 T. Wei, Z. Tang, Q. Yu and H. Chen, *ACS Appl. Mater. Interfaces*, 2017, **9**, 37511–37523.
- 14 L. Wang, C. Hu and L. Shao, *Int. J. Nanomed.*, 2017, **12**, 1227–1249.
- 15 A. Azam, A. S. Ahmed, M. Oves, M. S. Khan, S. S. Habib and A. Memic, *Int. J. Nanomed.*, 2012, **7**, 6003.
- 16 M. J. Hajipour, K. M. Fromm, A. Akbar Ashkarran, D. Jimenez de Aberasturi, I. R. de Larramendi, T. Rojo, V. Serpooshan, W. J. Parak and M. Mahmoudi, *Trends Biotechnol.*, 2012, **30**, 499–511.
- 17 C. A. Flemming and J. T. Trevors, *Water, Air, Soil Pollut.*, 1989, **44**, 143–158.
- 18 G. Benetti, E. Cavaliere, A. Canteri, G. Landini, G. M. Rossolini, L. Pallecchi, M. Chiodi, M. J. Van Bael, N. Winckelmans, S. Bals and L. Gavioli, *APL Mater.*, 2017, **5**, 036105.
- 19 Y. Cai, D. Wu, X. Zhu, W. Wang, F. Tan, J. Chen, X. Qiao and X. Qiu, *Ceram. Int.*, 2017, **43**, 1066–1072.
- 20 U. Bogdanović, V. Vodnik, M. Mitrić, S. Dimitrijević, S. D. Škapin, V. Žunić, M. Budimir and M. Stoiljković, *ACS Appl. Mater. Interfaces*, 2015, **7**, 1955–1966.
- 21 T. J. Webster and I. Seil, *Int. J. Nanomed.*, 2012, 2767.
- 22 U. Bogdanović, S. Dimitrijević, S. D. Škapin, M. Popović, Z. Rakočević, A. Leskovic, S. Petrović, M. Stoiljković and V. Vodnik, *Mater. Sci. Eng., C*, 2018, **93**, 49–60.
- 23 G. Hu, F. Nitze, E. Gracia-Espino, J. Ma, H. R. Barzegar, T. Sharifi, X. Jia, A. Shchukarev, L. Lu, C. Ma, G. Yang and T. Wågberg, *Nat. Commun.*, 2014, **5**, 5253.
- 24 A. V. Singh, V. Vyas, R. Patil, V. Sharma, P. E. Scopelliti, G. Bongiorno, A. Podestà, C. Lenardi, W. N. Gade and P. Milani, *PLoS One*, 2011, **6**, e25029.
- 25 S. Rtimi, S. Giannakis and C. Pulgarin, *Molecules*, 2017, **22**, 1074.
- 26 A. V. Singh, M. Ferri, M. Tamplenizza, F. Borghi, G. Divitini, C. Ducati, C. Lenardi, C. Piazzoni, M. Merlini, A. Podestà and P. Milani, *Nanotechnology*, 2012, **23**, 475101.
- 27 E. Cavaliere, S. De Cesari, G. Landini, E. Riccobono, L. Pallecchi, G. M. Rossolini and L. Gavioli, *Nanomedicine*, 2015, **11**, 1417–1423.
- 28 A. K. Suresh, D. A. Pelletier and M. J. Doktycz, *Nanoscale*, 2013, **5**, 463–474.
- 29 J. P. Ruparelia, A. K. Chatterjee, S. P. Duttagupta and S. Mukherji, *Acta Biomater.*, 2008, **4**, 707–716.
- 30 M. Valodkar, S. Modi, A. Pal and S. Thakore, *Mater. Res. Bull.*, 2011, **46**, 384–389.
- 31 A. A. Marakushev and N. I. Bezmen, *Int. Geol. Rev.*, 1971, **13**, 1781–1794.
- 32 K. Yliniemi, M. Vahvaselkä, Y. V. Ingelgem, K. Baert, B. P. Wilson, H. Terry and K. Kontturi, *J. Mater. Chem.*, 2008, **18**, 199–206.
- 33 S. Calderon Velasco, A. Cavaleiro and S. Carvalho, *Prog. Mater. Sci.*, 2016, **84**, 158–191.
- 34 P. Carvalho, P. Sampaio, S. Azevedo, C. Vaz, J. P. Espinós, V. Teixeira and J. O. Carneiro, *Appl. Surf. Sci.*, 2014, **307**, 548–557.
- 35 E. Cavaliere, G. Benetti, G. L. Celardo, D. Archetti, P. Pingue, G. Ferrini and L. Gavioli, *J. Nanopart. Res.*, 2017, **19**, 311.
- 36 G. L. Celardo, D. Archetti, G. Ferrini, L. Gavioli, P. Pingue and E. Cavaliere, *Mater. Res. Express*, 2017, **4**, 015013.
- 37 C. Schulte, A. Podestà, C. Lenardi, G. Tedeschi and P. Milani, *Acc. Chem. Res.*, 2017, **50**, 231–239.
- 38 J. Fischer, D. Pröfrock, N. Hort, R. Willumeit and F. Feyerabend, *Mater. Sci. Eng., B*, 2011, **176**, 830–834.
- 39 R. Ferrando, J. Jellinek and R. L. Johnston, *Chem. Rev.*, 2008, **108**, 845–910.
- 40 D. Bochicchio and R. Ferrando, *Phys. Rev. B: Condens. Matter Mater. Phys.*, 2013, **87**, 165435.
- 41 M. A. Jabbareh and F. Monji, *CALPHAD: Comput. Coupling Phase Diagrams Thermochem.*, 2018, **60**, 208–213.
- 42 T. Jin and Y. He, *J. Nanopart. Res.*, 2011, **13**, 6877–6885.
- 43 C. Dong, J. Cairney, Q. Sun, O. L. Maddan, G. He and Y. Deng, *J. Nanopart. Res.*, 2010, **12**, 2101–2109.
- 44 C. D. Wagner, *Handbook of x-ray photoelectron spectroscopy: a reference book of standard data for use in x-ray photoelectron spectroscopy*, Perkin-Elmer, 1979.
- 45 P. Kumari and P. Majewski, *J. Nanomater.*, 2013, **2013**, 1–7.
- 46 A. V. Singh, M. Galluzzi, F. Borghi, M. Indrieri, V. Vyas, A. Podestà and W. N. Gade, *J. Nanosci. Nanotechnol.*, 2013, **13**, 77–85.
- 47 A. V. Singh, V. Vyas, T. S. Salve, D. Cortelli, D. Dellasega, A. Podestà, P. Milani and W. N. Gade, *Biofabrication*, 2012, **4**, 025001.
- 48 M. Chiodi, E. Cavaliere, I. Kholmanov, M. de Simone, O. Sakho, C. Cepek and L. Gavioli, *J. Nanopart. Res.*, 2010, **12**, 2645–2653.
- 49 G. Benetti, M. Gandolfi, M. J. Van Bael, L. Gavioli, C. Giannetti, C. Caddeo and F. Banfi, *ACS Appl. Mater. Interfaces*, 2018, **10**, 27947–27954.
- 50 C. Caddeo, C. Melis, A. Ronchi, C. Giannetti, G. Ferrini, R. Rurali, L. Colombo and F. Banfi, *Phys. Rev. B: Condens. Matter Mater. Phys.*, 2017, **95**, 085306.

- 51 C. Giannetti, F. Banfi, D. Nardi, G. Ferrini and F. Parmigiani, *IEEE Photonics J.*, 2009, **1**, 21–32.
- 52 F. Banfi, F. Pressacco, B. Revaz, C. Giannetti, D. Nardi, G. Ferrini and F. Parmigiani, *Phys. Rev. B: Condens. Matter Mater. Phys.*, 2010, **81**, 155426.
- 53 P. V. AshaRani, G. Low Kah Mun, M. P. Hande and S. Valiyaveetil, *ACS Nano*, 2009, **3**, 279–290.
- 54 A. R. Gliga, S. Skoglund, I. Odnevall Wallinder, B. Fadeel and H. L. Karlsson, *Part. Fibre Toxicol.*, 2014, **11**, 11.
- 55 S. Tanuma, C. J. Powell and D. R. Penn, *Surf. Interface Anal.*, 1993, **20**, 77–89.
- 56 W. Vervisch, C. Mottet and J. Goniakowski, *Phys. Rev. B: Condens. Matter Mater. Phys.*, 2002, **65**, 245411.
- 57 R. Ferrando, G. Rossi, A. C. Levi, Z. Kuntová, F. Nita, A. Jelea, C. Mottet, G. Barcaro, A. Fortunelli and J. Goniakowski, *J. Chem. Phys.*, 2009, **130**, 174702.
- 58 D. Bochicchio, R. Ferrando, E. Panizon and G. Rossi, *J. Phys.: Condens. Matter*, 2016, **28**, 064005.
- 59 J. D. Loike, A. Plitt, K. Kothari, J. Zumeris, S. Budhu, K. Kavalus, Y. Ray and H. Jacob, *PLoS One*, 2013, **8**, e68334.